Available online at www.sciencedirect.com
ScienceDirect
Comput. Methods Appl. Mech. Engrg. 325 (2017) 314–329
Computer methods in applied mechanics and engineering
www.elsevier.com/locate/cma

Topology optimization of multiphase architected materials for energy dissipation

Alireza Asadpoure[a], Mazdak Tootkaboni[a], Lorenzo Valdevit[b,*]

[a] Department of Civil and Environmental Engineering, University of Massachusetts Dartmouth, Dartmouth, MA 02747, USA
[b] Department of Mechanical and Aerospace Engineering, University of California Irvine, Irvine, CA 92697, USA

Received 15 October 2016; received in revised form 17 May 2017; accepted 9 July 2017
Available online 13 July 2017

Highlights

- Topology optimization of multiphase architected materials for energy dissipation.
- Novel strategies for the interpolation of material properties in topology optimization.
- Efficient tools for estimating damping capacity and stiffness of multiphase materials.
- Multiphase cellular materials topologies for single and multiple target frequencies.
- Superior hybrid cellular topologies with high stiffness and damping and low density.

Abstract

In this article, we study the computational design of multiphase architected materials comprising a stiff phase, a dissipative phase, and void space, with enhanced vibration damping characteristics under wave propagation. We develop a topology optimization framework that maximizes a figure of merit comprising of effective stiffness, density and effective damping. We also propose novel material interpolation strategies to avoid the blending of different phases at any given point in the design domain. This is achieved by carefully defining different penalization schemes for different components of the merit function. The effective stiffness of the periodic multiphase material is calculated using homogenization theory and the Bloch–Floquet theorem is used to obtain its damping capacity, allowing for the investigation of the effect of wave directionality, material microarchitecture and intrinsic material properties on the wave attenuation characteristics. It is shown that the proposed topology optimization framework allows for systematic tailoring of microstructure of the multiphase materials for wide ranges of frequencies and densities and results in the identification of optimized multiphase cellular designs with void space that are superior to fully dense topologies.

Keywords: Topology optimization; Multiphase cellular materials; Dissipative materials; Optimal damping; Architected materials; Bloch–Floquet theorem

* Corresponding author.
E-mail address: valdevit@uci.edu (L. Valdevit).

http://dx.doi.org/10.1016/j.cma.2017.07.007
0045-7825/

1. Introduction

Recent advances in additive manufacturing processes, e.g. direct metal manufacturing and stereolithography [1], two-photon-polymerization Direct Laser Writing [2], and Self-Propagating Photopolymer Waveguide (SPPW)-based processing [3], have allowed fabrication of single- or multi-phase cellular materials with unit cell topologies of unprecedented complexity. These advances fueled significant activities in the area of optimal design of material micro-architectures [4], leading to the demonstration of a number of optimally designed architected materials with unprecedented combination of properties. Examples include materials with high specific stiffness and strength at low densities [5–7], superelastic graphene-based cellular monoliths [8] and lightweight recoverable metallic and ceramic nanolattices [9–11].

Among different material design objectives, design for vibration damping is one that has garnered a lot of attention in recent years, mainly because of its wide range of applications, from alleviation of seismic and wind response in buildings, to reducing noise and vibration in engines, climate control systems, commercial airplanes and passenger vehicles. To meet this particular objective, ideal combinations of high stiffness, low density and high loss coefficient are desirable, as they result in high natural frequencies – which prevent vibration under typical low frequency environmental stimuli – and high dissipation [12]. As these attributes are not available in a single monolithic material, recourse has to be made to multiphase materials, such as composites [13–15] or architected cellular materials that are designed by optimizing the geometric parameters of lattice-like architectures [16]. While designing material micro-architectures based on predefined lattice topologies often allows for analytical descriptions of the performance metric in terms of lattice parameters (thereby simplifying the design process), the heavy reliance on the intuition of the designer in the selection of lattice topology and the small design space associated with such an approach result in sub-optimal material designs. An alternative is to use the powerful technique of topology optimization, whereby an optimal arrangement of phases within the design domain is sought – with the help of computational optimizers – to maximize a desired performance metric under prescribed constraints. This technique has been extensively utilized in optimization of multiphase materials; see for example the pioneering work of Sigmund [17, 18] and Sigmund and Torquato [19] on designing periodic material microstructures with prescribed or extreme properties, known as inverse homogenization, the more recent works by Guest and Prévost [20] on design of materials with maximized stiffness and fluid permeability, Zhou and Li [21] on materials with extreme bulk modulus or extreme thermal conductivity, Prasad and Diaz [22] on design of viscoelastic materials with elastic moduli that softens with frequency and Zhou et al. [23] on design of metamaterials with negative permeability. Nevertheless, the application of topology optimization to meet more complex objectives in multiphase material systems, such as enhancing dynamic properties in the context of energy dissipation and wave propagation, is still in its infancy. To date, most of the studies in this area have aimed at designing materials that avoid wave propagation over a range of frequencies by introducing bandgaps [24–26], without requiring any material damping. Damping optimization in the presence of stiffness constraints was recently considered by Andreassen and Jensen [27], although this work was limited to design spaces populated by two-phase topologies.

In this paper, we lay out the elements of a topology optimization framework that aims at designing multiphase cellular materials with enhanced damping characteristics through combining a stiff phase (a metal or a ceramic), a dissipative phase (an elastomer) and void space. The organization of this paper is as follows. Section 2 discusses the basics of the optimization problem. This includes the figure of merit used as the objective function (Section 2.1), and strategies for the interpolation of material properties and enforcement of length scale in the context of multiphase topology optimization (Section 2.2). We then recall the basics of the Bloch–Floquet theory to analyze the dispersion characteristics and estimate the damping capacity of the periodic material architectures (Section 3.1), and homogenization theory to estimate the effective stiffness of the cellular materials (Section 3.2). Section 4 presents the details of sensitivity analysis, a crucial step to lay the ground for the utilization of efficient gradient-based optimizers. Section 5 discusses, in detail, how the proposed framework is used for optimal design of multiphase cellular materials with enhanced damping properties for both single and multiple target frequencies. This is followed by the concluding remarks in Section 6.

2. The optimization problem

2.1. Problem statement

We begin by choosing the performance metric for optimal design of the multiphase cellular material to be based on dynamical properties of plates. From vibration theory, it is known that the natural frequency of a plate scales

with $E^{1/3}/\varrho$, where E and ϱ are the elastic modulus and density of the constituent material, respectively [28]. Maximizing the lowest natural frequency is a natural approach for vibration control under low-frequency, narrow-band environmental stimuli. Under broad-band excitation with high frequency content this approach is ineffective. In these situations, maximization of the intrinsic damping capacity of the material ($\tan\delta$) is the most viable strategy. In this work, we combine both approaches and choose $E^{1/3}\tan\delta/\varrho$ as the figure of merit for vibration control. Although the numerical results we present are clearly specific to this choice, we emphasize that the methods described herein are fully general and equally applicable to a variety of alternative figures of merit. By discretizing the design domain (Ω) with finite elements, the binary optimization problem associated with the optimal design of an n_{ph}-phase architected material is formally stated as follows:

$$\max_{\boldsymbol{\rho}} \quad \frac{E^{\frac{1}{3}}\tan\delta}{\varrho} \tag{1}$$

$$s.t. \quad \rho_p^e = \begin{cases} 1 & \text{if element } e \text{ contains phase } p \\ 0 & \text{otherwise} \end{cases} \qquad e \in \Omega, \;\; p = 1, 2, \ldots, n_{ph} \tag{2}$$

$$\varrho_{min} \leq \varrho \leq \varrho_{max} \tag{3}$$

$$\sum_{p=1}^{n_{ph}} \rho_p^e = 1 \quad e \in \Omega \tag{4}$$

where ρ_p^e is a design variable defining if element e contains phase p, $\rho_p^e = 1$, or not, $\rho_p^e = 0$, ϱ_{min} and ϱ_{max} are the lower and upper limits for desired material density, respectively, and $\boldsymbol{\rho} = \{\rho_p^e\}$ is the vector of design variables. Eq. (4) guarantees that each element contains one and only one phase. It also indicates that only $n_{ph} - 1$ independent design variables are required to fully determine each element's phase. In this paper, we study optimal design of three-phase architected materials ($n_{ph} = 3$) composed of a stiff phase, a lossy phase, and a void phase requiring two design variables per element to define the optimization problem. However, we emphasize that the framework presented in the following sections can be readily extended to any number of phases $n_{ph} > 3$ and other figures of merit. Nevertheless, an appropriately formulated optimization problem that is not overly restrictive on the design space is essential in ensuring the existence of a feasible solution. The feasible region in the formulation presented in Eqs. (1)–(4), for example, encompasses any binary solution satisfying the density constraint in Eq. (3).

2.2. Material interpolation, penalization and mapping

The design domain for the optimization problem defined by Eqs. (1)–(4) is usually discretized into a large of number of finite elements n_{el}. The total number of design variables, $n_{el} \times n_{ph}$, can become relatively large, when high-resolution optimal solutions are of interest. To efficiently solve the associated high dimensional optimization problem, we follow the common approach of relaxing the binary constraints in Eq. (2) [29,30] and allow the design variables to take on any intermediate values between 0 and 1. While this would allow for the utilization of gradient-based optimizers, thus significantly increasing the efficiency of the design process which often involves multiple design trials, it calls for a material model that respects the non-binary nature of design variables as well as a strategy to push the intermediate design variables to their bounds, i.e. 0 and 1. We propose the following interpolation with penalization for intermediate values, which is a modification of the interpolation proposed by Sigmund and Torquato [19], and model the void phase as a very soft material with ρ_1^e representing the design variable for this phase for element e

$$E^e\left(\rho_1^e, \rho_2^e\right) = \rho_1^e E_1 + \left(1-\rho_1^e\right)^{P_E}\left(\rho_2^{e\,P_E} E_2 + \left(1-\rho_2^e\right)^{P_E} E_3\right) \tag{5}$$

$$\varrho^e\left(\rho_1^e, \rho_2^e\right) = \rho_1^e \varrho_1 + \left(1-\rho_1^e\right)^{P_M}\left(\rho_2^{e\,P_M}\varrho_2 + \left(1-\rho_2^e\right)^{P_M}\varrho_3\right) \tag{6}$$

where E_p and ϱ_p are elastic modulus and density of phase p, respectively, and P_E and P_M are the exponents penalizing the intermediate values. It is noted that P_E should be large enough, for example 5, to dramatically reduce (penalize) E^e for intermediate values of $(1-\rho_1^e)\rho_2^e$ making these values inefficient. It is also noted that, in Eq. (5), there is no penalty exponent for ρ_1^e in the first term on right hand side. We propose to drop the exponent because phase one is the void phase and is modeled as an ultra soft phase whose stiffness keeps the global stiffness matrix positive definite (this property is needed for calculation of effective moduli explained in Section 3.2). On the other hand, one can penalize

(increase) ϱ^e for intermediate values of $(1-\rho_1^e)\rho_2^e$ in Eq. (6) by using a small enough positive number for the exponent P_M, for example $1/P_E$. This penalization increases the element density ϱ^e and the density of the material occupying the design domain (ϱ in Eq. (1)), compared with the case with no penalization when intermediate design variables could develop within the domain. From interpolations given by Eqs. (5)–(6), if $\rho_1^e = 1$ element e contains the first phase regardless of the value of ρ_2^e. On the other hand, if $\rho_1^e = 0$ then element e contains the second phase as long as $\rho_2^e = 1$ or the third phase if $\rho_2^e = 0$. Such interpolations automatically satisfy Eq. (4) and this equation is therefore not enforced in the optimization process. Furthermore, to arrive at better solutions, that is solutions with design variables closer to binary values, the parameter $\tan\delta$ can also be penalized for intermediate values of ρ_p^e in $\boldsymbol{\rho}$. This is explained in Section 3.1. Finally, in order to circumvent numerical instabilities (see e.g. Sigmund and Petersson [31]) and also to improve manufacturability of optimized designs, we impose a minimum length scale to features developed within the design domain. There exist a number of techniques [32–35] for controlling the length scale of the topological features in the final design. In this work, we use the Heaviside Projection Method (HPM) proposed by Guest et al. [36] with its modification [37] and adapt it for multiphase projection. In HPM, the design variables are mapped from a set of independent variables, $\boldsymbol{\phi} = \{\phi_p^j\}$ as follows

$$\rho_p^e = \mathrm{H}\left(\mu_p^e\left(\boldsymbol{\phi}_p\right)\right), \quad p = 1, 2; \quad \boldsymbol{\phi}_p = \{\phi_p^j\}; \quad j = 1, 2, \ldots, n_{\phi_p} \tag{7}$$

where H is the Heaviside function, n_{ϕ_p} is the number of independent design variables for phase p, and μ_p^e is a weighted average of independent variables $\boldsymbol{\phi}_p$ within radius r_{min_p} of the center of element e defined by

$$\mu_p^e\left(\boldsymbol{\phi}_p\right) = \frac{\sum_{j\in N_p^e} \phi_p^j w_p\left(\mathbf{x}_{\phi_p^j} - \mathbf{x}^e\right)}{\sum_{j\in N_p^e} w_p\left(\mathbf{x}_{\phi_p^j} - \mathbf{x}^e\right)}, \quad N_p^e = \{j : \|\mathbf{x}_{\phi_p^j} - \mathbf{x}^e\| < r_{min_p}\} \tag{8}$$

where $\mathbf{x}_{\phi_p^j}$ is the location of independent design variable ϕ_p^j, $\mathbf{x}^e$ is the location of the centroid of element e, and w_p is a weighting function defined by

$$w_p(\mathbf{x}) = 1 - \frac{\|\mathbf{x}\|}{r_{min_p}} \tag{9}$$

where $\|\bullet\|$ denotes L^2-norm of $\bullet$. Considering definitions given by Eqs. (8)–(9), any positive ϕ_p^j projects phase p onto elements within its r_{min_p} distance by making their μ_p^e value greater than zero. Eq. (7) then maps such positive μ_p^e values to unit values for ρ_p^e, which is equivalent to having phase p within these elements. To be able to benefit from the efficiency of gradient-based optimizers, HPM utilizes the following regularized version of the Heaviside step function to map the independent design variables, $\boldsymbol{\phi}$, to design variables, $\boldsymbol{\rho}$ [36]

$$\rho_p^e\left(\boldsymbol{\phi}_p\right) = \mathrm{H}\left(\mu_p^e\left(\boldsymbol{\phi}_p\right)\right) = 1 - \exp\left(-\beta\mu_p^e\left(\boldsymbol{\phi}_p\right)\right) + \mu_p^e\left(\boldsymbol{\phi}_p\right)\exp\left(-\beta\right) \tag{10}$$

where β is a shape parameter dictating the transition between a linear mapping, when $\beta = 0$, and the Heaviside step function, as $\beta \to \infty$; see e.g. Guest et al. [37] for a detailed discussion on this parameter.

3. Estimation of effective properties

3.1. Effective damping of multiphase periodic media

A crucial step in solving the optimization problem defined in Eqs. (1)–(4) is calculating the material damping represented by $\tan\delta$. To this end, we study wave propagation in a viscoelastic medium with periodic microstructure and its attenuation. Dynamic equilibrium for such a medium takes the following form:

$$\nabla\cdot\mathbf{C}(\mathbf{x}) : \nabla_{sym}\left(\mathbf{u}(\mathbf{x}, t)\right) = \varrho(\mathbf{x})\,\ddot{\mathbf{u}}(\mathbf{x}, t) \tag{11}$$

where $\varrho(\mathbf{x})$ is the material mass density at point $\mathbf{x}$, $\mathbf{u}(\mathbf{x}, t)$ is displacement vector at point $\mathbf{x}$ and time t, $\mathbf{C}(\mathbf{x})$ is the stiffness tensor at point $\mathbf{x}$, $\ddot{\mathbf{u}}(\mathbf{x}, t)$ is the second derivative of displacement with respect to time t, and ∇_{sym} denotes the symmetric gradient operator. For a periodic medium under harmonic oscillation, the Bloch [38] and Floquet [39] theorems provide a solution to Eq. (11) of the form:

$$\mathbf{u}(\mathbf{x}, t) = \tilde{\mathbf{u}}(\mathbf{x})\exp\left(i\mathbf{k}^T\mathbf{x} + i\omega t\right) \tag{12}$$

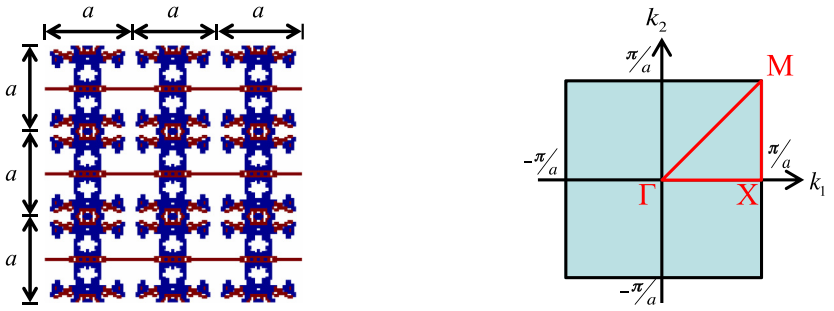

(a) 3 × 3 unit cell. (b) First Brillouin zone.

Fig. 1. (a) A 2D square unit cell of length a in a 3 × 3 arrangement with three different phases; each color represents a different phase; (b) first Brillouin zone for a square unit cell of length a. (For interpretation of the references to colour in this figure legend, the reader is referred to the web version of this article.)

where i is the unit imaginary number, i.e. $i = \sqrt{-1}$, ω is the frequency of the harmonic oscillation, $\mathbf{k}$ is the wave vector and $\tilde{\mathbf{u}}(\mathbf{x})$ is an Ω-periodic function with Ω the design domain, i.e. the unit cell of the periodic material. Full discovery of the wave propagation characteristics in a material with a periodic microstructure requires obtaining the dispersion curves only within the first Brillouin zone in $\mathbf{k}$-space. The first Brillouin zone for a d-dimensional periodic unit cell of length a is $[-\pi/a \quad \pi/a]^d$. Fig. 1(a), for example, shows a 3 × 3 arrangement of a 2-dimensional periodic material. Each color in this figure represents a different phase. For this periodic material, the first Brillouin zone in 2-dimensional $\mathbf{k}$-space is a square defined by $[-\pi/a \quad \pi/a]^2$ as shown in Fig. 1(b). The symmetry of unit cell can be exploited to reduce the calculation of dispersion curves to a subregion within the first Brillouin zone. For a unit cell with square symmetry this subregion becomes the red triangle in Fig. 1(b). It is common practice in the literature to only report dispersion curves along the perimeter of the triangle, i.e., the path $\Gamma - X - M - \Gamma$.

Substituting Eq. (12) into Eq. (11) leads to an eigenvalue problem. Finite element discretization of the unit cell turns this eigenvalue problem to one that involves the components of the wave vector (k_1 and k_2 in two dimensions) and frequency (ω). Following a $\mathbf{k}(\omega)$-formulation [40] this eigenvalue problem reads as follows:

$$\left(\mathbf{K}_k\left(\omega, \mathbf{n}, \boldsymbol{\phi}\right) - k\left(\omega, \mathbf{n}, \boldsymbol{\phi}\right)\mathbf{M}_k\left(\omega, \mathbf{n}, \boldsymbol{\phi}\right)\right)\mathbf{d}_k\left(\omega, \mathbf{n}, \boldsymbol{\phi}\right) = \mathbf{0} \tag{13}$$

where $\mathbf{K}_k$, $\mathbf{M}_k$, and $\mathbf{d}_k$ are *equivalent* stiffness matrix, mass matrix and displacement vector, respectively, $\mathbf{k} = k\mathbf{n}$ with $\mathbf{n}$ a unit vector with the desired direction within the first Brillouin zone and k is the wave number. Eq. (13) can be solved for the first n_{ev} eigenvalues, which represent wavenumbers for different branches of the dispersion curve.

Modeling dissipative materials as having complex elastic moduli, the wave vectors (the solutions to Eq. (13)) become also complex with imaginary parts that represent a damped response, i.e. a spatially decaying wave. For such waves, the damping coefficient ($\tan\delta$) can be estimated by Cremer et al. [41]

$$\tan\delta\left(\omega, \mathbf{n}, \boldsymbol{\phi}\right) = 2\frac{\text{Im}\ (k)}{\text{Re}\ (k)}\left(\omega, \mathbf{n}, \boldsymbol{\phi}\right) \tag{14}$$

where Re (•) and Im (•) denote real and imaginary parts of •, respectively. The advantage of using the above formulation is that it can be easily applied to materials whose properties are frequency dependent. In computing $\tan\delta$ using Eqs. (13)–(14), we propose to penalize (reduce) the value of damping coefficient for intermediate values of $\boldsymbol{\rho}$ through the following interpolation

$$\begin{aligned} E^e\left(\rho_1^e, \rho_2^e\right) = &\text{Re}\left(\rho_1^e E_1 + \left(1-\rho_1^e\right)\left(\rho_2^e E_2 + \left(1-\rho_2^e\right)E_3\right)\right) \\ &+ i\text{Im}\left(\rho_1^e E_1 + \left(1-\rho_1^e\right)^{P_E}\left(\rho_2^{eP_E} E_2 + \left(1-\rho_2^e\right)^{P_E} E_3\right)\right). \end{aligned} \tag{15}$$

The interpolation above reduces the imaginary part of the modulus for intermediate values of $\boldsymbol{\rho}$ leading to a smaller damping coefficient when forming $\mathbf{K}_k$ and $\mathbf{M}_k$. However, care is needed when interpolating the density of elements using Eq. (6) as penalization with $P_M \neq 1$ may lead to $\tan\delta$ values that are higher than those for no penalization in Eq. (15). To circumvent such pathological cases, when forming and assembling $\mathbf{K}_k$ and $\mathbf{M}_k$, we propose to interpolate densities with $P_M = 1$.

It is finally worth mentioning that using the interpolation proposed in Eq. (5) instead of Eq. (15) for estimating damping coefficient would potentially promote a mixture of phases in the optimized solutions, and hence poor phase separation. It can be shown that at low volume fractions of the stiff phase, the modified SIMP method, i.e. Eq. (5), overestimates the effective damping coefficient compared to the case of no penalization, thus assigning phase mixtures a higher efficiency. Conversely, the proposed interpolation scheme, i.e. Eq. (15), will always penalize a mixture of phases at each point by reducing the effective damping coefficient, thus promoting better phase separation. Even more importantly, it can be shown that one can achieve better phase separation through more aggressive penalization by simply increasing the penalty exponent in Eq. (15).

3.2. Effective stiffness

In order to obtain effective stiffness of periodic cellular materials, we use the homogenization approach. Since its development [42–44] and early numerical implementations [45], homogenization has been extensively employed in topology optimization to numerically obtain the macroscopic properties of periodic media; see e.g. Hassani and Hinton [46,47,48] for a review of the method and its applications in topology optimization. We here present only the relevant equations from the finite element implementation of homogenization approach as applied to computing effective elastic properties. The effective axial modulus in the ith direction, $\bar{E}_i(\boldsymbol{\phi})$, as a function of the components of homogenized compliance tensor, $\mathbf{S}^H(\boldsymbol{\phi}) = \left[S^H_{ij}(\boldsymbol{\phi})\right]$, reads

$$\bar{E}_i(\boldsymbol{\phi}) = \frac{1}{S^H_{ii}(\boldsymbol{\phi})}; \quad i = \begin{cases} 1,2 & \text{in 2D} \\ 1,2,3 & \text{in 3D.} \end{cases} \tag{16}$$

The homogenized compliance tensor, $\mathbf{S}^H$ in $\boldsymbol{\epsilon} = \mathbf{S}^H\boldsymbol{\sigma}$ with $\boldsymbol{\sigma}$ and $\boldsymbol{\epsilon}$ the stress and strain tensors respectively, can be obtained by inverting the homogenized stiffness tensor, $\mathbf{C}^H(\boldsymbol{\phi}) = \left[C^H_{ij}(\boldsymbol{\phi})\right]$, i.e. $\mathbf{S}^H(\boldsymbol{\phi}) = \mathbf{C}^{H^{-1}}(\boldsymbol{\phi})$. One can obtain the components of the homogenized stiffness tensor using the finite element analysis as

$$C^H_{ij}(\boldsymbol{\phi}) = \frac{1}{V^{\Omega}} \sum_{e\in\Omega} \left(\mathbf{d}^{e(i)}_0 - \mathbf{d}^{e(i)}(\boldsymbol{\phi})\right)^T \mathbf{k}^e(\boldsymbol{\phi}) \left(\mathbf{d}^{e(j)}_0 - \mathbf{d}^{e(j)}(\boldsymbol{\phi})\right); \quad i,j = \begin{cases} 1,2,3 & \text{in 2D} \\ 1,2,\ldots,6 & \text{in 3D} \end{cases} \tag{17}$$

where V^{Ω} is the total volume of elements within the design domain, $\mathbf{k}^e(\boldsymbol{\phi})$ is the stiffness matrix of element e that is a function of design variables $\boldsymbol{\phi}$ through Eqs. (5) and (10), $\mathbf{d}^{e(i)}_0$ is the nodal displacement vector for element e associated with the ith unit test strain, and $\mathbf{d}^{e(i)}(\boldsymbol{\phi})$ is the elemental part of the Ω-periodic displacement vector $\mathbf{d}^{(i)}(\boldsymbol{\phi})$ for element e, which can be obtained by solving the following linear system of equations

$$\mathbf{K}(\boldsymbol{\phi})\,\mathbf{d}^{(i)}(\boldsymbol{\phi}) = \mathbf{f}^{(i)}(\boldsymbol{\phi}); \quad i = \begin{cases} 1,2,3 & \text{in 2D} \\ 1,2,\ldots,6 & \text{in 3D} \end{cases} \tag{18}$$

where $\mathbf{K}(\boldsymbol{\phi})$ is the stiffness matrix obtained by assembling all the elemental stiffness matrices, and $\mathbf{f}^{(i)}(\boldsymbol{\phi})$ is the load vector associated with the ith unit test strain, i.e.

$$\mathbf{f}^{(i)}(\boldsymbol{\phi}) = \mathop{\mathsf{A}}_{e\in\Omega} \mathbf{k}^e(\boldsymbol{\phi})\,\mathbf{d}^{e(i)}_0; \quad i = \begin{cases} 1,2,3 & \text{in 2D} \\ 1,2,\ldots,6 & \text{in 3D} \end{cases} \tag{19}$$

with $\mathop{\mathsf{A}}_{e\in\Omega}$ denoting assembly over all elements. It is worth mentioning that the test strains can be any combinations of three or six independent strain fields for two- or three-dimensional problems, respectively. For simplicity, as mentioned above, one can use three unit test strains for two-dimensional problems, consisting of two independent unit axial strains and one unit shear strain, or six unit test strains for three-dimensional problems, consisting of three independent unit axial strains and three independent unit shear strains.

4. Sensitivity analysis

To calculate the sensitivities of the performance metric and constraints (see Sections 2.1 and 5) with respect to design variables, the sensitivities of the damping coefficient, $\tan\delta$, and the effective axial modulus, $\bar{E}_i$, are needed.

The sensitivity of the damping coefficient with respect to the independent design variables, $\boldsymbol{\phi} = \{\phi_p^j\}$, reads

$$\frac{d\,(\tan\delta)}{d\phi_p^j} = 2\frac{\mathrm{Re}\,(k)\mathrm{Im}\left(\frac{dk}{d\phi_p^j}\right) - \mathrm{Im}\,(k)\mathrm{Re}\left(\frac{dk}{d\phi_p^j}\right)}{\mathrm{Re}\,(k)^2} \tag{20}$$

where for simplicity we have dropped the dependence of $\tan\delta$ and k on ω, $\mathbf{n}$, and $\boldsymbol{\phi}$. In order to find derivatives of k with respect to ϕ_p^j, we take the derivatives of Eq. (13) with respect to this variable. Premultiplying the result by the left eigenvectors of the same eigen-problem (the solution to $\tilde{\mathbf{d}}_k^T(\mathbf{K}_k - k\mathbf{M}_k) = \mathbf{0}$) and further simplifications lead to

$$\frac{dk}{d\phi_p^j} = \frac{\tilde{\mathbf{d}}_k^T\left(\frac{d\mathbf{K}_k}{d\phi_p^j} - k\frac{d\mathbf{M}_k}{d\phi_p^j}\right)\mathbf{d}_k}{\tilde{\mathbf{d}}_k^T\mathbf{M}_k\mathbf{d}_k}. \tag{21}$$

It is noted that the need for solving one extra eigen-problem for the left eigenvectors arises due to the fact that $\mathbf{K}_k$ is not Hermitian. The derivative of $\mathbf{K}_k$ and $\mathbf{M}_k$ in Eq. (21) with respect to ϕ_p^j can be obtained using the chain rule

$$\frac{d\mathbf{K}_k}{d\phi_p^j} = \mathop{\mathsf{A}}_{e\in N_p^j}\left(\frac{d\mathbf{K}_k^e}{dE^e}\frac{dE^e}{d\phi_p^j} + \frac{d\mathbf{K}_k^e}{d\varrho^e}\frac{d\varrho^e}{d\phi_p^j}\right) \tag{22}$$

$$\frac{d\mathbf{M}_k}{d\phi_p^j} = \mathop{\mathsf{A}}_{e\in N_p^j}\frac{d\mathbf{M}_k^e}{dE^e}\frac{dE^e}{d\phi_p^j} \tag{23}$$

where $\mathbf{K}_k^e$ and $\mathbf{M}_k^e$ are *equivalent* stiffness and mass matrices for element e. Detailed steps toward obtaining derivatives of $\mathbf{K}_k^e$ and $\mathbf{M}_k^e$ with respect to E^e and ϱ^e can be found in Andreassen and Jensen [40]. Furthermore, $dE^e/d\phi_p^j$ and $d\varrho^e/d\phi_p^j$ can be obtained using the chain rule as follows

$$\frac{dE^e}{d\phi_p^j} = \frac{dE^e}{d\rho_p^e}\frac{d\rho_p^e}{d\mu_p^e}\frac{d\mu_p^e}{d\phi_p^j} \tag{24}$$

$$\frac{d\varrho^e}{d\phi_p^j} = \frac{d\varrho^e}{d\rho_p^e}\frac{d\rho_p^e}{d\mu_p^e}\frac{d\mu_p^e}{d\phi_p^j} \tag{25}$$

where derivatives of E^e and ϱ^e with respect to ρ_p^e are straightforward to compute and can be obtained by taking the derivatives of Eqs. (15) and (6), respectively, and $d\rho_p^e/d\mu_p^e$ and $d\mu_p^e/d\phi_p^j$ take the following form by taking the derivatives of Eqs. (10) and (8), respectively

$$\frac{d\rho_p^e}{d\mu_p^e} = \beta\exp\left(-\beta\mu_p^e\right) + \exp\left(-\beta\right) \tag{26}$$

$$\frac{d\mu_p^e}{d\phi_p^j} = \frac{w_p\left(\mathbf{x}_{\phi_p^j} - \mathbf{x}^e\right)}{\sum_{i\in N_p^e} w_p\left(\mathbf{x}_{\phi_p^i} - \mathbf{x}^e\right)}. \tag{27}$$

On the other hand, the derivative of the effective axial moduli with respect to independent design variables can be obtained by computing the derivatives of Eq. (16) as follows

$$\frac{d\bar{E}_i}{d\phi_p^j} = \frac{-1}{\left(S_{ii}^H\right)^2}\frac{dS_{ii}^H}{d\phi_p^j} \tag{28}$$

where sensitivity of S_{ii}^H with respect to ϕ_p^j can be obtained by taking the derivative of the homogenized stiffness tensor, that is

$$\frac{d\mathbf{S}^H}{d\phi_p^j} = -\mathbf{S}^H\frac{d\mathbf{C}^H}{d\phi_p^j}\mathbf{S}^H \tag{29}$$

Table 1
Elastic modulus (E_i), density (ϱ_i), damping coefficient ($\tan\delta_i$), Poisson's ratio (ν_i), and phase number, used in Eqs. (5)–(6) and (15), of the ultra-soft phase, the stiff phase, and the dissipative phase.

Phase	E_i (GPa)	ϱ_i (kg/m^3)	$\tan\delta_i \times 10^{-2}$	ν_i	Phase number
Dissipative	1.0	1210	10	0.3	1
Stiff	100	4500	0.1	0.3	2
Ultra-soft	0.001	1	0.001	0.3	3

where $d\mathbf{C}^H/d\phi_p^j$ takes the following form using the chain rule, the adjoint method, and Eq. (17)

$$\frac{dC_{ij}^H}{d\phi_p^j} = \frac{1}{V^\Omega}\sum_{e\in N_p^j}\left(\mathbf{d}_0^{e(i)} - \mathbf{d}^{e(i)}\right)^T \frac{d\mathbf{k}^e}{dE^e}\left(\mathbf{d}_0^{e(j)} - \mathbf{d}^{e(j)}\right)\frac{dE^e}{d\phi_p^j}. \tag{30}$$

In the above equation, computing $d\mathbf{k}^e/dE^e$ is straightforward since $\mathbf{k}^e$ is a linear function of E^e under linear mechanics assumptions.

5. Optimal design for damping

The optimization framework discussed in Section 2 is used to study optimal topologies for 2D periodic three-phase cellular materials consisting of a stiff phase, a dissipative phase and a void phase, with the objective of minimizing the figure of merit in Eq. (1). For computational purposes, we model the void phase as an ultra-soft phase compared to the other two phases. The elastic modulus, density, damping coefficient, and Poisson's ratio used in Eqs. (5)–(6) and (15), are displayed in Table 1. Square unit cells of length a with two perpendicular symmetry lines passing through the center are considered. The optimization problem defined in Eqs. (1)–(4), augmented with the required constraints discussed in Section 2 can be written in the following form:

$$\max_{\boldsymbol{\phi}} \quad \frac{\bar{E}_1^{\frac{1}{3}}\,(P_E \geq 1)\,\min_{i,j}\tan\delta_{ij}\,(P_E \geq 1,\, P_M = 1)}{\bar{\varrho}\,(P_M \leq 1)}, \quad i = 1, 2, \ldots, n_f, \;\; j = 1, 2, \ldots, n_{ev} \tag{31}$$

$$s.t. \quad \left(\mathbf{K}_k\,(\omega_i, \mathbf{n}, \boldsymbol{\phi}) - k_{ij}\,(\omega_i, \mathbf{n}, \boldsymbol{\phi})\,\mathbf{M}_k\,(\omega_i, \mathbf{n}, \boldsymbol{\phi})\right)\mathbf{d}_k\,(\omega_i, \mathbf{n}, \boldsymbol{\phi}) = \mathbf{0} \tag{32}$$

$$\tan\delta_{ij}\,(\omega_i, \mathbf{n}, \boldsymbol{\phi}) = 2\frac{\mathrm{Im}\,(k_{ij})}{\mathrm{Re}\,(k_{ij})}\,(\omega_i, \mathbf{n}, \boldsymbol{\phi}) \tag{33}$$

$$\varrho_{min} \leq \bar{\varrho}\,(P_M = 1) \leq \varrho_{max} \tag{34}$$

$$0 \leq \phi_p^j \leq 1, \quad p = 1, 2, \;\; j = 1, 2, \ldots, n_{\phi_p} \tag{35}$$

where n_f is the number of frequencies considered and $\bar{\varrho}$ is the density of the material estimated as:

$$\bar{\varrho} = \frac{\sum_{e=1}^{n_{el}} v^e \varrho^e}{\sum_{e=1}^{n_{el}} v^e} \tag{36}$$

where v^e is the volume of element e and ϱ^e should be computed using Eq. (6) with a penalization exponent (P_M). It is noted that while, as discussed before, an exponent smaller than or equal to 1, e.g. $P_M = 1/P_E$, is used in Eq. (31) to penalize elements with a mixture of phases, $P_M = 1$ should be used to estimate the density of the unit cell in Eq. (34). The purpose of Eq. (34) is to seek optimized cellular material topologies for a range of densities between the minimum density and maximum density of constituent materials, that is $\varrho_{min}, \varrho_{max} \in [\min(\varrho_p) \;\; \max(\varrho_p)]$ with $p = 1, 2, \ldots, n_{\phi_p}$. It is also noted that the min function in front of the damping coefficient in Eq. (31) is used to ensure that the proposed figure of merit is optimized for the worst case scenario, i.e. the minimum value among all damping coefficients corresponding to all frequencies and branches of the dispersion curve. Furthermore, waves considered in this study are 1D waves propagating in the horizontal direction, that is $\mathbf{n}^T = [1\ 0\ 0]$ and $\mathrm{Re}\,(k_{ij})$ lies between 0 and π/a within the first Brillouin zone, i.e. on the $\Gamma - X$ line. Moreover, for some frequencies and wave directions, it is possible for Eq. (32) to have fewer eigenvalues than n_{ev}. In this case, the extra indices in Eq. (31) are ignored. Finally, the maximum value for damping coefficient computed through Eq. (33) is restricted to 1.0 to avoid inaccurate estimation of damping capacity by Eq. (14) for $\tan\delta$ values greater than one.

In computing $\bar{E}_1$ in Eq. (31), Eq. (16) is utilized along with the penalization proposed in Eq. (5). On the other hand, we use Eq. (15) for elastic modulus and Eq. (6) with no penalization for density in assembling $\mathbf{K}_k$ and $\mathbf{M}_k$ and solving the eigenvalue problem in Eq. (32). This would penalize mixture of phases in each element and avoid overestimating damping coefficient through Eq. (33). The Method of Moving Asymptotes (MMA) proposed by Svanberg [49,50] is used as the gradient based optimizer. For each optimization problem, the optimizer starts from a random initial guess. The results presented in the rest of the paper correspond to the best solution among a few optimized unit cells for each set of frequencies and density ranges. This is done to make the optimization process less prone to getting stuck in local minima. Moreover, we use a 50 by 50 element mesh and a minimum length scale equal to the size of each element. Using two symmetry lines, the total number of independent variables required to optimize the topology of the three-phase unit cells becomes 1352 which, as mentioned before, are located at the nodes of elements.

5.1. Design for a single target frequency

In this section, we study material microstructures optimized for a single frequency value in the 1 kHz–200 kHz range ($\omega a/\sqrt{E_1/\varrho_1} \in [0.011 \quad 2.2]$). The optimization problem defined by Eqs. (31)–(34) with $n_f = 1$ is solved for waves propagating horizontally and twenty density values with $\bar{\varrho}/\varrho_1 \in [0.33 \quad 3.3]$. Table 2 displays optimized microstructures in 3×3 unit cell arrangements, which represent the value of design variables ($\boldsymbol{\rho}$) without any rounding to near binary values. It is seen that all three phases, including stiff, dissipative, and void phases develop within the unit cell. The emergence of all three phases including the void phase in all optimized designs, for all combinations of density and frequency values, confirms the superiority of the cellular and multiphase material microarchitecture designs over two-phase designs with no void features. Furthermore, it is seen that interpolation through Eqs (5)–(6) and (15) with judiciously chosen penalization exponents (P_M and P_E) leads to a good phase separation in spite of starting with a random initial guess that translates to a mixture of phases for the elements within the discretized unit cell. The solid phases, however, are not always connected within the optimal solutions as the void phase is modeled as an ultra soft material. This issue can be avoided by, for example, introducing a permeability constraint on solid phases' topology, circumventing the development of islands of solids surrounded by the ultra-soft material (see e.g. Andreassen and Jensen [27]).

Figs. 2(a) and 2(b) show contour plots of the proposed performance metric for damping capacity of optimized microstructures, including those illustrated in Table 2 for different target frequencies and density values. The difference between these two figures is that in plotting Fig. 2(b) optimized unit cells for which the performance metric is likely to be a local minimum are filtered. An optimized solution is identified as a likely local minimum if it has a figure of merit lower than that of two optimized microstructures that pertain to either (a) the same frequency and a lower and higher density or (b) the same target density and a lower and higher frequency. This filtering strategy is used in plotting the rest of the contour plots in this paper. It is seen in Fig. 2(b) that the metric increases for low density microstructures and a better performance can be achieved for higher frequencies. Moreover, as can be seen in Fig. 3, while at lower densities significant improvement in the performance metric can be achieved through manipulation of specific stiffness, $\bar{E}^{1/3}/\bar{\varrho}$, it is the change (increase) in damping coefficient, $\tan\delta$, that achieves better performance metric for higher target frequencies. Finally, Fig. 4 illustrates dispersion curves on the $\Gamma - X - M - \Gamma$ line within the first Brillouin zone for four different microstructures that are optimized for wave vectors on the $\Gamma - X$ line for relatively low density and low frequency in Fig. 4(a), high density and low frequency in Fig. 4(b), low density and high frequency in Fig. 4(c) and high density and high frequency in Fig. 4(d). While the band structure for these microstructures are different, it is seen that no clear band gaps develop on the $\Gamma - X$ line; that is there is an intersection between the dashed line corresponding to the target frequency for which the microstructure is optimized and the dispersion curves from Γ to X. This is likely a result of limiting the damping coefficient to 1. It is, however, worth mentioning that a high $\tan\delta$ value in the absence of a clear band gap can be achieved by creating a scenario where the target frequency intersects as few branches of dispersion curve as possible on the $\Gamma - X$ line, ideally one.

The Ashby chart of the specific stiffness, $E^{1/3}/\varrho$, against the damping coefficient, $\tan\delta$, for different materials including the optimized microstructures is shown in Fig. 5. It is seen that for target frequencies, the optimized microstructures populate mostly the top right of the chart representing a region that pertains to the best values of the figure of merit. Furthermore, notice that the performance of most optimized multiphase microarchitectures is far superior to those of the individual solid phases, clearly illustrating the advantage of architected designs. A natural question emerges as to the importance of the void space in the performance of the optimized microstructures: is the

Table 2
Optimized microstructures in a 3 × 3 unit cell arrangement for different target densities and single-frequencies. Stiff, dissipative, and ultra-soft phases are shown in red, blue, and white colors, respectively.

$\omega a/\sqrt{E_1/\varrho_1}$ \ $\bar{\varrho}/\varrho_1$	0.45	0.83	1.7	2.5	2.9
0.22	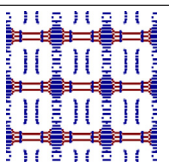	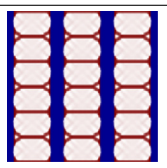	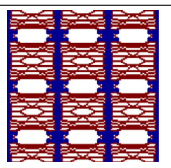	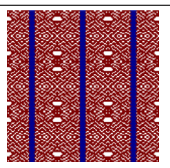	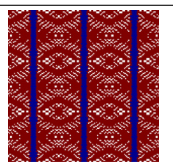
0.44	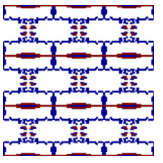	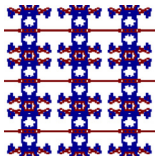	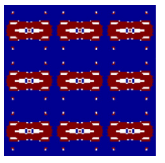	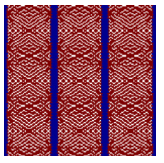	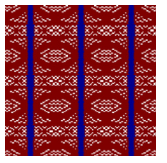
1.10	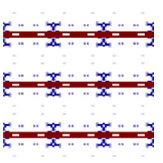	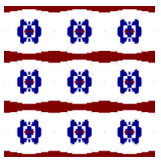	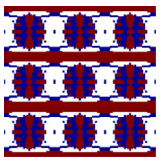	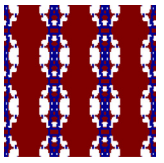	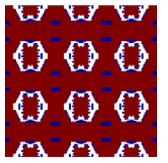
1.65	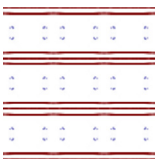	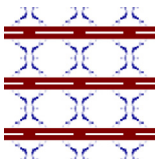	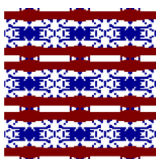	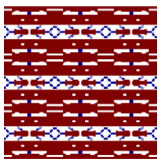	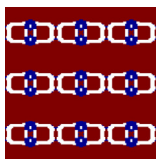

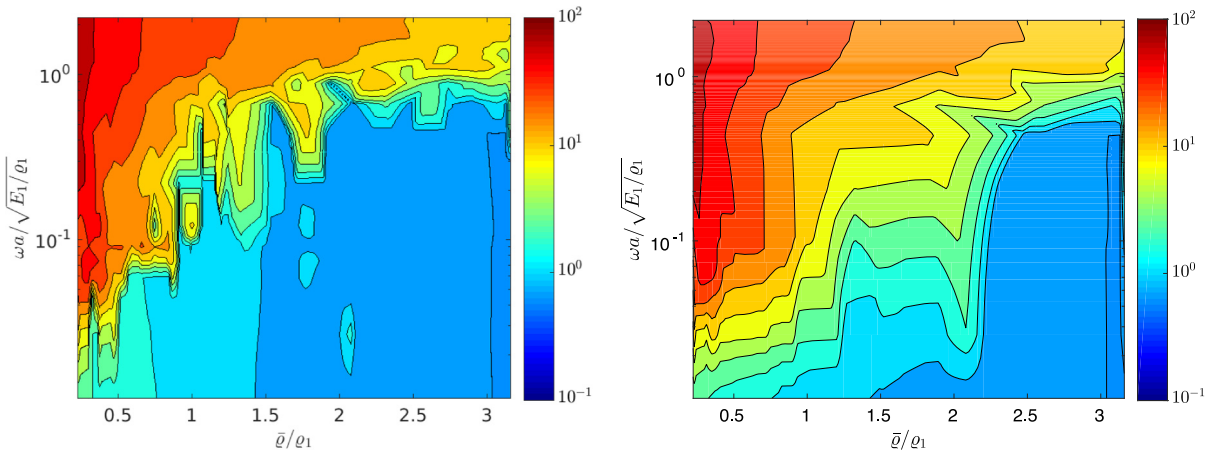

(a) Full (including local mimina). (b) Filtered.

Fig. 2. The normalized figure of merit for optimized three-phase microstructures for different target densities and single-frequencies consisting of (a) all points and (b) all points except likely local minima. The figure of merit is normalized against the corresponding value for the dissipative phase.

presence of void space essential in order to achieve superior values of the figure of merit, or can similar values be obtained with a fully dense two-phase material? In order to quantitatively answer this question, we optimize microstructures consisting of only the stiff and dissipative phases. Fig. 6 displays the contour plot of the merit function for the optimized solutions. As can be seen, the figure of merit drastically decreases when compared with those displayed in Fig. 2(b). This signifies the importance of cellular designs – that is allowing for the void phase

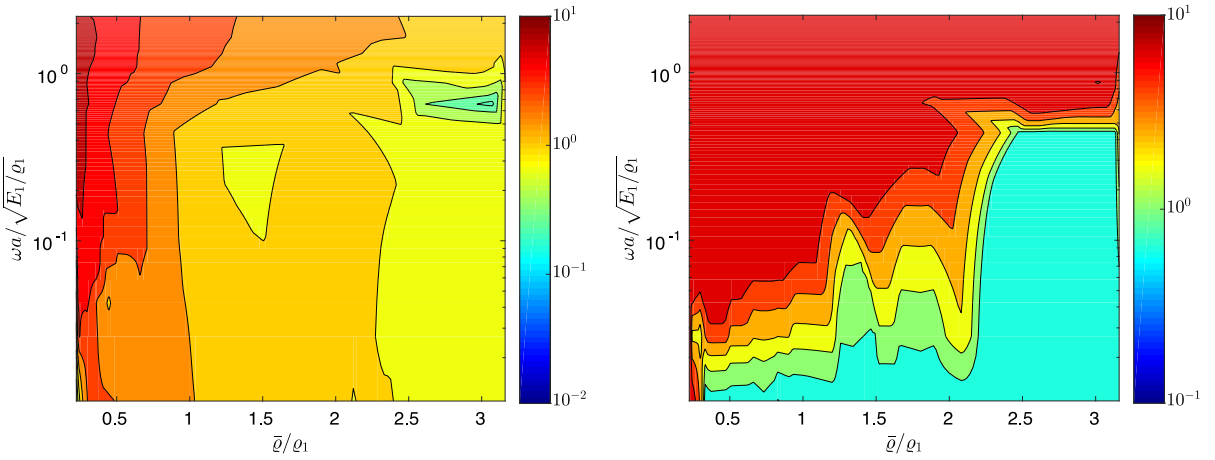

(a) Normalized specific stiffness.

(b) Normalized damping coefficient.

Fig. 3. The normalized (a) specific stiffness, $\bar{E}_1^{\frac{1}{3}}/\bar{\varrho}$, and (b) damping coefficient, $\min_{i,j} \tan\delta_{ij}$, of optimized microstructures for different target densities and single-frequencies. In each figure, normalization is done against the corresponding value for the dissipative phase.

to be developed – in improving the damping performance of the designed microstructures compared to fully solid designs. It is finally worth mentioning that this important finding (which has significant implications for the design of multi-phase materials) was entirely enabled by the development of the novel interpolation strategies proposed above.

5.2. *Design for multiple target frequencies*

A careful analysis of the optimized microstructures presented in preceding section reveals superior damping performance only within a narrow frequency band around the target design frequency. The solid line in Fig. 7, for example, shows the variation of merit function versus frequency for a microstructure that has been optimized for a single-frequency $\omega a/\sqrt{E_1/\varrho_1} = 2.2$ and $\bar{\varrho}/\varrho_1 = 1.9$. It is seen from this figure that, while a maximum performance of $19.4(E_1^{1/3}\tan\delta_1/\varrho_1)$ can be achieved at the target frequency, this performance drops by more than 80% for a 12% change in frequency around the design frequency. One way to avoid such a dramatic drop is to design the microstructure for a range of frequencies. The dashed line in Fig. 7 shows the variation of the performance metric for a microstructure optimized for four frequencies, $n_f = 4$, with $\omega a/\sqrt{E_1/\varrho_1} \in [1.9 \quad 2.2]$ and for $\bar{\varrho}/\varrho_1 = 1.9$. It is seen that the optimized microstructure this time maintains a minimum damping coefficient of $10\tan\delta_1$ within this interval and a slightly smaller specific stiffness compared to the single-frequency design leading to a normalized performance metric of about 18. This is only 6.7% below that of the optimized microstructure for the single-frequency which is indicative of how topology optimization for multiple target frequencies is able to arrive at more robust designs – that is designs that maintain a high performance for a wide range of frequencies – through dramatically changing the topology of the material microstructure.

Fig. 8 depicts how the topology of the microstructure optimized for a range of frequencies ($\omega a/\sqrt{E_1/\varrho_1} \in [1.9 \quad 2.2]$) and the associated figure of merit change with target density. It is seen that, similar to single-frequency design, all three phases develop in the optimized microstructures, thus confirming the superiority of multiphase cellular material designs. Furthermore, the proposed penalization strategies have clearly been able to achieve phase separation within the material microstructure. The variation of figure of merit with respect to density is also similar to the one observed for single-frequency designs indicating that, for multiple frequency designs too, the best performance pertains to the lightest microstructures made of a stiff phase, a lossy phase and void space.

6. Concluding remarks

This paper presents a framework for optimizing the microstructure of multiphase cellular materials consisting of a stiff phase, a lossy phase and void space, optimized for energy dissipation. The material microstructure is optimized

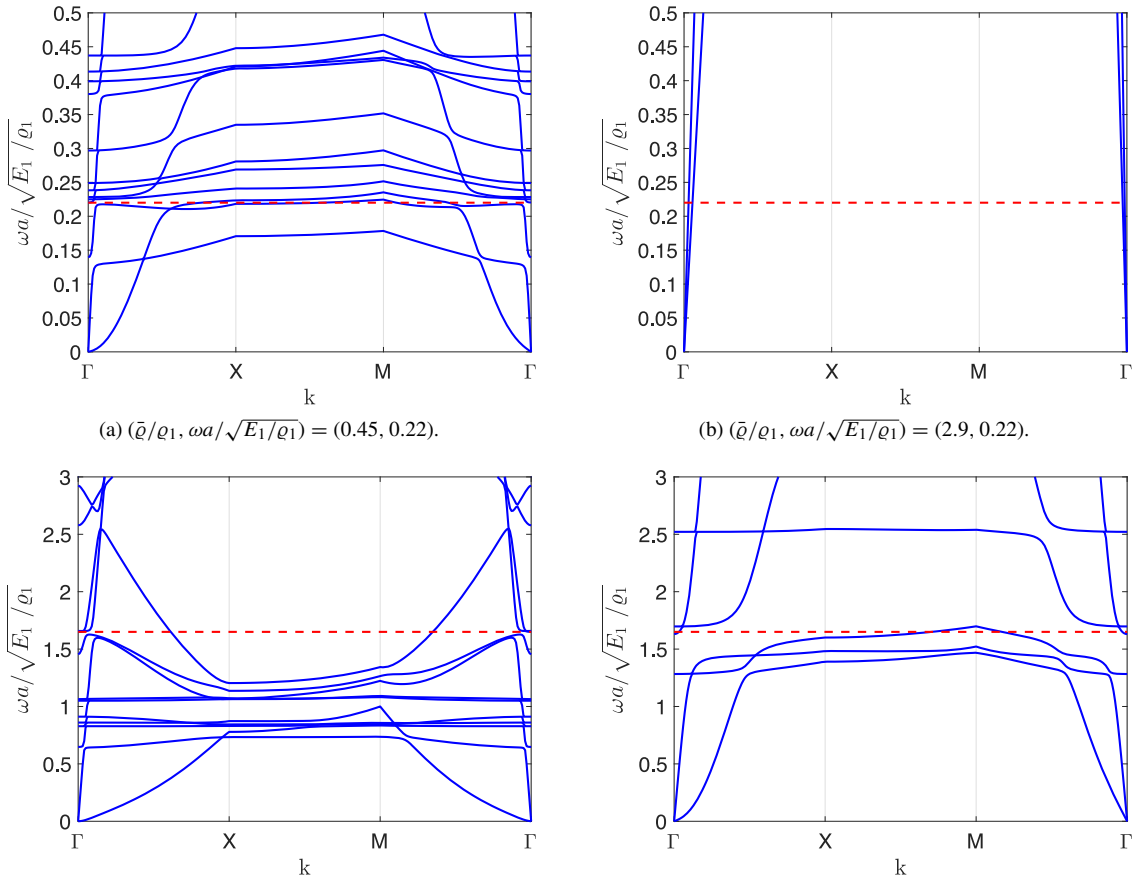

(a) $(\bar{\varrho}/\varrho_1, \omega a/\sqrt{E_1/\varrho_1}) = (0.45, 0.22)$.

(b) $(\bar{\varrho}/\varrho_1, \omega a/\sqrt{E_1/\varrho_1}) = (2.9, 0.22)$.

(c) $(\bar{\varrho}/\varrho_1, \omega a/\sqrt{E_1/\varrho_1}) = (0.45, 1.65)$.

(d) $(\bar{\varrho}/\varrho_1, \omega a/\sqrt{E_1/\varrho_1}) = (2.9, 1.65)$.

Fig. 4. Dispersion curves for four different microstructures optimized for wave vectors on $\Gamma - X$ line for relatively (a) low density and low frequency, (b) high density and low frequency, (c) low density and high frequency and (d) high density and high frequency. The dashed line in each figure displays the frequency for which the microstructure is optimized.

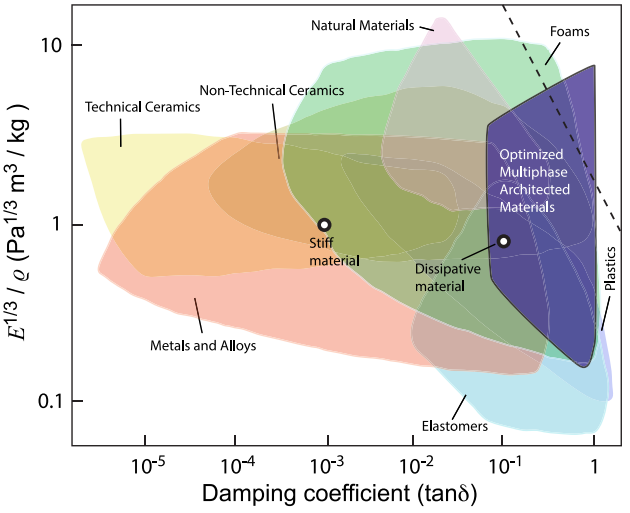

Fig. 5. Ashby chart of the damping coefficient, $\tan\delta$, against the specific stiffness, $E^{1/3}/\varrho$, for different materials including the optimized microstructures.

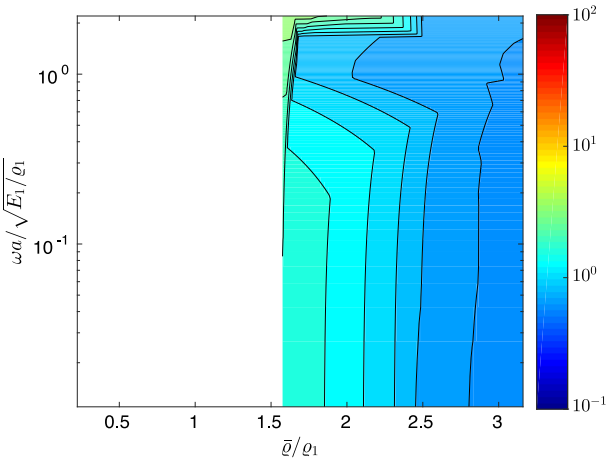

Fig. 6. The normalized figure of merit of two-phase optimized microstructures, (stiff and dissipative phases), for different target densities and single-frequencies. The figure of merit is normalized against the corresponding value for the dissipative phase.

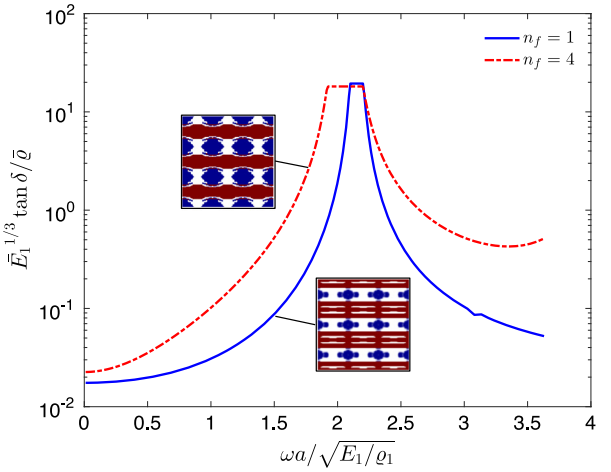

Fig. 7. Variation of normalized figure of merit by frequency for two optimized microstructures; solid line: design for single frequency with $\omega a/\sqrt{E_1/\varrho_1} = 2.2$, dashed line: design for four frequencies with $\omega a/\sqrt{E_1/\varrho_1} \in [1.9 \quad 2.2]$. The figure of merit is normalized against the corresponding value for the dissipative phase and $\bar{\varrho}/\varrho_1 = 1.9$.

for a classical figure of merit in vibration damping of plates, which is a combination of high stiffness, low density and high damping coefficient. The Bloch–Floquet theorem is used to estimate the damping capacity of the periodic multiphase microstructure and homogenization theory is used to calculate the effective stiffness of the periodic media. The optimization process starts by assigning each element within the design domain a mixture of all three phases. Judiciously chosen material interpolation schemes and penalization strategies are then introduced to converge to near binary final topologies. Design sensitivities associated with these new interpolation schemes are also derived to allow for the use of gradient-based optimizers.

The proposed framework is used for optimizing the microstructure of multiphase periodic materials for wave attenuation at a prescribed frequency and unidirectional waves along the horizontal direction (i.e., tracing the $\Gamma - X$ path in the first Brillouin zone). This results in multiphase cellular material topologies that possess distinct phase boundaries, demonstrating that the penalization strategies adopted can successfully separate the phases. The best performance metric is achieved for high target frequencies and low target densities. However, the damping performance for these single-frequency-designed microstructures may deteriorate when waves with slightly different frequencies from the target frequency propagate within the medium. To address this, the optimization framework is

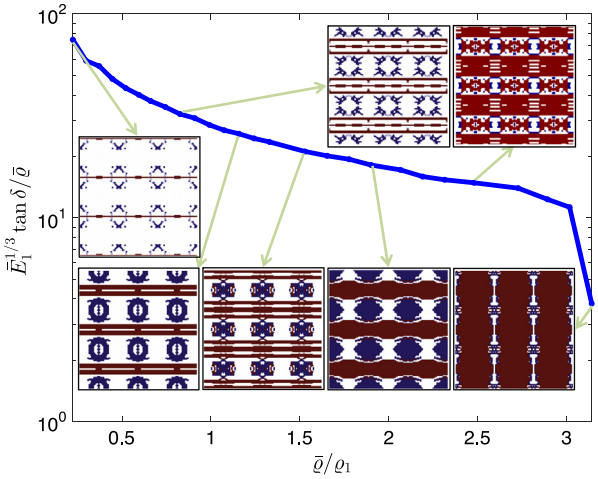

Fig. 8. Normalized figure of merit versus target density for microstructures optimized for four frequencies, $n_f = 4$, with $\omega a/\sqrt{E_1/\varrho_1} \in [1.9 \quad 2.2]$. The figure of merit is normalized against the corresponding value for the dissipative phase. Stiff, dissipative and ultra-soft phases in optimized microstructures are shown in red, blue, and white colors, respectively. (For interpretation of the references to colour in this figure legend, the reader is referred to the web version of this article.)

used to design multiphase materials for a range of frequencies in the neighborhood of a target frequency. This leads to multi-phase material topologies that maintain high performance over a wider range of frequencies making them more robust to small frequency disturbances. Our results clearly indicate that properly optimized multi-phase cellular materials outperform single or multi-phase dense materials in energy dissipation through optimal juxtaposition of the lossy phase and void space within the stiff matrix. Recent improvements in additive manufacturing strategies can produce the multi-phase architectures described in this article, albeit in a fully polymeric system.

Acknowledgments

This work was financially supported by the Office of Naval Research under Grant No. N00014-11-1-0884 (program manager: D. Shifler). This support is gratefully acknowledged. Asadpoure and Tootkaboni also acknowledge partial support from UMassD and NSF under Grant No. CMMI-1401575, respectively. The authors are also thankful to Krister Svanberg for providing the MMA optimizer subroutine. The computing support was provided by the High Performance Computing Cluster within the Office of Information Technology at the University of California, Irvine.

References

[1] Ian Gibson, David W. Rosen, Brent Stucker, Additive Manufacturing Technologies, Springer US, Boston, MA, 2010. http://dx.doi.org/10.1007/978-1-4419-1120-9.

[2] Tommaso Baldacchini (Ed.), Three-dimensional Microfabrication Using Two-photon Polymerization: Fundamentals, Technology, and Applications, William Andrew, 2015, p. 485.

[3] Alan J. Jacobsen, William Barvosa-Carter, Steven Nutt, Micro-scale truss structures formed from self-propagating photopolymer waveguides, Adv. Mater. 19 (22) (2007) 3892–3896. http://dx.doi.org/10.1002/adma.200700797.

[4] N.A. Fleck, V.S. Deshpande, M.F. Ashby, Micro-architectured materials: past, present and future, in: Proceedings of the Royal Society of London a: Mathematical, Physical and Engineering Sciences, vol. 466, The Royal Society, 2010, pp. 2495–2516.

[5] Xiaoyu Zheng, Howon Lee, Todd H. Weisgraber, Maxim Shusteff, Joshua DeOtte, Eric B. Duoss, Joshua D. Kuntz, Monika M. Biener, Qi Ge, Julie a. Jackson, Sergei O. Kucheyev, Nicholas X. Fang, Christopher M. Spadaccini, Ultralight, ultrastiff mechanical metamaterials, Science 344 (6190) (2014) 1373–1377. http://dx.doi.org/10.1126/science.1252291.

[6] Jens Bauer, Almut Schroer, Ruth Schwaiger, Oliver Kraft, Approaching theoretical strength in glassy carbon nanolattices, Nature Mater. 15 (4) (2016) 438–443. http://dx.doi.org/10.1038/nmat4561.

[7] Jens Bauer, Almut Schroer, Ruth Schwaiger, Iwiza Tesari, Christian Lange, Lorenzo Valdevit, Oliver Kraft, Push-to-pull tensile testing of ultra-strong nanoscale ceramic-polymer composites made by additive manufacturing, Extreme Mech. Lett. 3 (2015) 105–112. http://dx.doi.org/10.1016/j.eml.2015.03.006.

[8] Ling Qiu, Jeffery Z. Liu, Shery L.Y. Chang, Yanzhe Wu, Dan Li, Biomimetic superelastic graphene-based cellular monoliths, Nature Commun. 3 (2012) 1241. http://dx.doi.org/10.1038/ncomms2251.

[9] Kevin J. Maloney, Christopher S. Roper, Alan J. Jacobsen, William B. Carter, Lorenzo Valdevit, Tobias A. Schaedler, Microlattices as architected thin films: Analysis of mechanical properties and high strain elastic recovery, APL Materials 1 (2) (2013) 022106. http://dx.doi.org/10.1063/1.4818168.
[10] Tobias A. Schaedler, Alan J. Jacobsen, Anna Torrents, Adam E. Sorensen, Jie Lian, Julia R. Greer, Lorenzo Valdevit, Wiliam B. Carter, Ultralight metallic microlattices, Science 334 (6058) (2011) 962–965. http://dx.doi.org/10.1126/science.1211649.
[11] Lucas R. Meza, Satyajit Das, Julia R. Greer, Strong, lightweight, and recoverable three-dimensional ceramic nanolattices, Science 345 (6202) (2014) 1322–1326. http://dx.doi.org/10.1126/science.1255908.
[12] Lorna J. Gibson, Michael F. Ashby, Cellular Solids: Structure and Properties, second ed., Cambridge University Press, UK, 1999, p. 532.
[13] Trisha Sain, Julien Meaud, Greg Hulbert, Ellen M. Arruda, Anthony M. Waas, Simultaneously high stiffness and damping in a class of wavy layered composites, Compos. Struct. 101 (2013) 104–110. http://dx.doi.org/10.1016/j.compstruct.2013.01.024.
[14] Julien Meaud, Trisha Sain, Gregory M. Hulbert, Anthony M. Waas, Analysis and optimal design of layered composites with high stiffness and high damping, Int. J. Solids Struct. 50 (9) (2013) 1342–1353. http://dx.doi.org/10.1016/j.ijsolstr.2013.01.014.
[15] Roderic S. Lakes, T. Lee, A. Bersie, Y.C. Wang, Extreme damping in composite materials with negative-stiffness inclusions, Nature 410 (6828) (2001) 565–567. http://dx.doi.org/10.1038/35069035.
[16] Ladan Salari-Sharif, Tobias A. Schaedler, Lorenzo Valdevit, Energy dissipation mechanisms in hollow metallic microlattices, J. Mater. Res. 29 (16) (2014) 1755–1770. http://dx.doi.org/10.1557/jmr.2014.226.
[17] Ole Sigmund, Materials with prescribed constitutive parameters: An inverse homogenization problem, Int. J. Solids Struct. 31 (17) (1994) 2313–2329. http://dx.doi.org/10.1016/0020-7683(94)90154-6.
[18] Ole Sigmund, Tailoring materials with prescribed elastic properties, Mech. Mater. 20 (4) (1995) 351–368. http://dx.doi.org/10.1016/0167-6636(94)00069-7.
[19] O. Sigmund, S. Torquato, Design of materials with extreme thermal expansion using a three-phase topology optimization method, J. Mech. Phys. Solids 45 (6) (1997) 1037–1067. http://dx.doi.org/10.1016/S0022-5096(96)00114-7.
[20] James K. Guest, Jean H. Prévost, Optimizing multifunctional materials: Design of microstructures for maximized stiffness and fluid permeability, Int. J. Solids Struct. 43 (22–23) (2006) 7028–7047. http://dx.doi.org/10.1016/j.ijsolstr.2006.03.001.
[21] Shiwei Zhou, Qing Li, Computational design of multi-phase microstructural materials for extremal conductivity, Comput. Mater. Sci. 43 (3) (2008) 549–564. http://dx.doi.org/10.1016/j.commatsci.2007.12.021.
[22] J. Prasad, A.R. Diaz, Viscoelastic material design with negative stiffness components using topology optimization, Struct. Multidiscip. Optim. 38 (6) (2009) 583–597. http://dx.doi.org/10.1007/s00158-008-0308-6.
[23] Shiwei Zhou, Wei Li, Yuhang Chen, Guangyong Sun, Qing Li, Topology optimization for negative permeability metamaterials using level-set algorithm, Acta Mater. 59 (7) (2011) 2624–2636. http://dx.doi.org/10.1016/j.actamat.2010.12.049.
[24] Ole Sigmund, Jakob S. Jensen, Systematic design of phononic band-gap materials and structures by topology optimization, Philos. Trans. R. Soc. Lond. Ser. A Math. Phys. Eng. Sci. 361 (1806) (2003) 1001–1019. http://dx.doi.org/10.1098/rsta.2003.1177.
[25] Søren Halkjaer, Ole Sigmund, Jakob S. Jensen, Inverse design of phononic crystals by topology optimization, Z. Kristallogr. 220 (9–10) (2005) 895–905. http://dx.doi.org/10.1524/zkri.2005.220.9-10.895.
[26] Kevin L. Manktelow, Michael J. Leamy, Massimo Ruzzene, Topology design and optimization of nonlinear periodic materials, J. Mech. Phys. Solids 61 (12) (2013) 2433–2453. http://dx.doi.org/10.1016/j.jmps.2013.07.009.
[27] Erik Andreassen, Jakob S. Jensen, Topology optimization of periodic microstructures for enhanced dynamic properties of viscoelastic composite materials, Struct. Multidiscip. Optim. 49 (5) (2014) 695–705. http://dx.doi.org/10.1007/s00158-013-1018-2.
[28] Michael F. Ashby, Materials Selection in Mechanical Design, second ed., Butterworth-Heinemann, 1999, p. 513.
[29] Martin P. Bendsøe, Ole Sigmund, Topology Optimization: Theory, Methods and Applications, Springer, 2003.
[30] Ole Sigmund, On the usefulness of non-gradient approaches in topology optimization, Struct. Multidiscip. Optim. (2011). http://dx.doi.org/10.1007/s00158-011-0638-7.
[31] Ole Sigmund, Joakim H. Petersson, Numerical instabilities in topology optimization: A survey on procedures dealing with checkerboards, mesh-dependencies and local minima, Struct. Optim. 16 (1) (1998) 68–75. http://dx.doi.org/10.1007/BF01214002.
[32] Joakim H. Petersson, Ole Sigmund, Slope constrained topology optimization, Internat. J. Numer. Methods Engrg. 41 (8) (1998) 1417–1434. http://dx.doi.org/10.1002/(SICI)1097-0207(19980430)41:8⟨1417::AID-NME344⟩3.0.CO;2-N.
[33] Tyler E. Bruns, Daniel A. Tortorelli, Topology optimization of non-linear elastic structures and compliant mechanisms, Comput. Methods Appl. Mech. Engrg. 190 (26–27) (2001) 3443–3459. http://dx.doi.org/10.1016/S0045-7825(00)00278-4.
[34] Thomas A. Poulsen, A new scheme for imposing a minimum length scale in topology optimization, Internat. J. Numer. Methods Engrg. 57 (6) (2003) 741–760. http://dx.doi.org/10.1002/nme.694.
[35] Ole Sigmund, Morphology-based black and white filters for topology optimization, Struct. Multidiscip. Optim. 33 (4–5) (2007) 401–424. http://dx.doi.org/10.1007/s00158-006-0087-x.
[36] James K. Guest, Jean H. Prévost, Ted B. Belytschko, Achieving minimum length scale in topology optimization using nodal design variables and projection functions, Internat. J. Numer. Methods Engrg. 61 (2) (2004) 238–254. http://dx.doi.org/10.1002/nme.1064.
[37] James K. Guest, Alireza Asadpoure, Seung-Hyun Ha, Eliminating beta-continuation from Heaviside projection and density filter algorithms, Struct. Multidiscip. Optim. (2011). http://dx.doi.org/10.1007/s00158-011-0676-1.
[38] Felix Bloch, Über die Quantenmechanik der Elektronen in Kristallgittern, Z. Phys. 52 (7–8) (1929) 555–600. http://dx.doi.org/10.1007/BF01339455.
[39] G. Floquet, Sur les équations différentielles linéaires à coefficients périodiques, Ann. Éc. Norm. Super. 12 (1883) 47–88.
[40] Erik Andreassen, Jakob S. Jensen, Analysis of phononic bandgap structures with dissipation, J. Vib. Acoust. 135 (4) (2013) 041015. http://dx.doi.org/10.1115/1.4023901.

[41] Lothar Cremer, Maria A. Heckl, Björn A.T. Petersson, Structure-Borne Sound, Springer, Berlin, Heidelberg, 2005. http://dx.doi.org/10.1007/b137728.
[42] Enrique Sanchez-Palencia, Non-Homogeneous Media and Vibration Theory, in: Lecture Notes in Physics, vol. 127, Springer, Berlin, Heidelberg, 1980. http://dx.doi.org/10.1007/3-540-10000-8.
[43] Alain Bensoussan, Jacques-Louis Lions, George Papanicolaou, Asymptotic Analysis for Periodic Structures, in: Studies in Mathematics and Its Applications, vol. 5, 1978.
[44] Doina Cioranescu, Jeannine Saint Jean Paulin, Homogenization in open sets with holes, J. Math. Anal. Appl. 71 (2) (1979) 590–607. http://dx.doi.org/10.1016/0022-247X(79)90211-7.
[45] JoséMiranda Guedes, Noboru Kikuchi, Preprocessing and postprocessing for materials based on the homogenization method with adaptive finite element methods, Comput. Methods Appl. Mech. Engrg. 83 (2) (1990) 143–198. http://dx.doi.org/10.1016/0045-7825(90)90148-F.
[46] Behrooz Hassani, Ernest S. Hinton, A review of homogenization and topology optimization I-homogenization theory for media with periodic structure, Comput. Struct. 69 (6) (1998) 707–717. http://dx.doi.org/10.1016/S0045-7949(98)00131-X.
[47] Behrooz Hassani, Ernest S. Hinton, A review of homogenization and topology opimization II-analytical and numerical solution of homogenization equations, Comput. Struct. 69 (6) (1998) 719–738. http://dx.doi.org/10.1016/S0045-7949(98)00132-1.
[48] Behrooz Hassani, Ernest S. Hinton, A review of homogenization and topology optimization III-topology optimization using optimality criteria, Comput. Struct. 69 (6) (1998) 739–756. http://dx.doi.org/10.1016/S0045-7949(98)00133-3.
[49] Krister Svanberg, The method of moving asymptotesa new method for structural optimization, Internat. J. Numer. Methods Engrg. 24 (2) (1987) 359–373. http://dx.doi.org/10.1002/nme.1620240207.
[50] Krister Svanberg, A globally convergent version of MMA without linesearch, in: Niels Olhoff, George I.N. Rozvany (Eds.), Proceedings of the First World Congress of Structural and Multidisciplinary Optimization, Pergamon Press, Elmsford, NY, 1995, pp. 6–16.